Slope failures along the deformation front of the Cascadia margin: linking slide morphology to subduction zone parameters

MICHAEL RIEDEL[1]*, MICHELLE M. CÔTÉ[2], MORELIA URLAUB[1], JACOB GEERSEN[1], NASTASJA A. SCHOLZ[3], KATHRIN NAEGELI[2] & GEORGE D. SPENCE[3]

[1]*GEOMAR Helmholtz Centre for Ocean Research Kiel, Wischhofstrasse 1–3, 24148 Kiel, Germany*

[2]*Natural Resources Canada, Geological Survey of Canada – Pacific, 9860 West Saanich Road, Sidney, BC, V8L 4B2, Canada*

[3]*School of Earth and Ocean Sciences, University of Victoria, Victoria, BC, V8P 5C2, Canada*

M.R., 0000-0001-5729-4482

Present address: K.T., Centre for Glaciology, Department of Geography and Earth Sciences, Aberystwyth University, Aberystwyth SY23 3DB, UK

**Correspondence: mriedel@geomar.de*

Abstract: Marine acoustic data are used to map and characterize submarine slope failure along the accretionary prism of Cascadia. Two main styles of slope failure are identified: (1) failures with curved head scarps, which are predominantly associated with incoherent debris-flow deposits; and (2) failures with rectangular head scarps, which are predominantly associated with intact sediment blocks. Rectangular head scarps mostly occur on thrust ridges with slope angles <16° and ridge heights <650 m, whereas curved head scarps occur predominantly on steeper and higher ridges. Off Vancouver Island, failure style and head-scarp geometry also change with ridge azimuth. We propose that the curved head scarps and debris flows may be a result of higher kinetic forcing of the downsliding sediments and a higher degree of mixing. At the more gently sloped, less elevated ridges, the kinetic forcing may be smaller, which leads to intact failure masses. Extensional faults at ridges with curved scarps may result from oversteepening and collapse of the sediments that cannot withstand their own weight due to limited internal shear strength. The slide geometries and potential controls on failure style may inform subsequent studies in assessing the risks for tsunami generation from submarine slope failures along the Cascadia margin.

Submarine slope failures are a frequent phenomenon on continental margins. On active accretionary margins, they often cumulate along the deformation front and the most seawards-located thrust ridges of the accretionary prism (e.g. McAdoo & Watts 2004); but failure type, size and morphology often varies along a single margin (e.g. Mulder & Cochonat 1996; McAdoo *et al.* 2000; Twichell *et al.* 2009). The first recognition of submarine slope failures off Cascadia dates back to seafloor imaging with the SEAMARK-II system (e.g. Davis *et al.* 1987; Davis & Hyndman 1989), and the GLORIA seafloor backscatter imagery off the coasts of Washington and Oregon (Grim *et al.* 1991). Additional attention to slope failures off Vancouver Island was raised after high-resolution EM300 multibeam mapping along northern Cascadia revealed numerous additional slide complexes (Kelley & Delaney 2005). Using sedimentary data from cores targeting these failures, Hamilton *et al.* (2015) reconstructed a history of past megathrust earthquakes off Vancouver Island based on the dating of turbidites. An initial summary of these slope failures along northern Cascadia was completed by Riedel *et al.* (2016*b*). In contrast to the northern Cascadia margin, substantial work on slope failures has been undertaken along the southern Cascadia margin off the coasts of Oregon and Washington. Investigations included understanding the geomorphology of failures, linkages to fluid flow and submarine canyon systems (Orange & Breen 1992; McAdoo *et al.* 1997, 2000; Goldfinger *et al.* 2000; McAdoo & Watts 2004). Studies

From: Lintern, D. G., Mosher, D. C., Moscardelli, L. G., Bobrowsky, P. T., Campbell, C., Chaytor, J. D., Clague, J. J., Georgiopoulou, A., Lajeunesse, P., Normandeau, A., Piper, D. J. W., Scherwath, M., Stacey, C. & Turmel, D. (eds) 2019. *Subaqueous Mass Movements*. Geological Society, London, Special Publications, **477**, 47–67.
First published online April 27, 2018, https://doi.org/10.1144/SP477.33

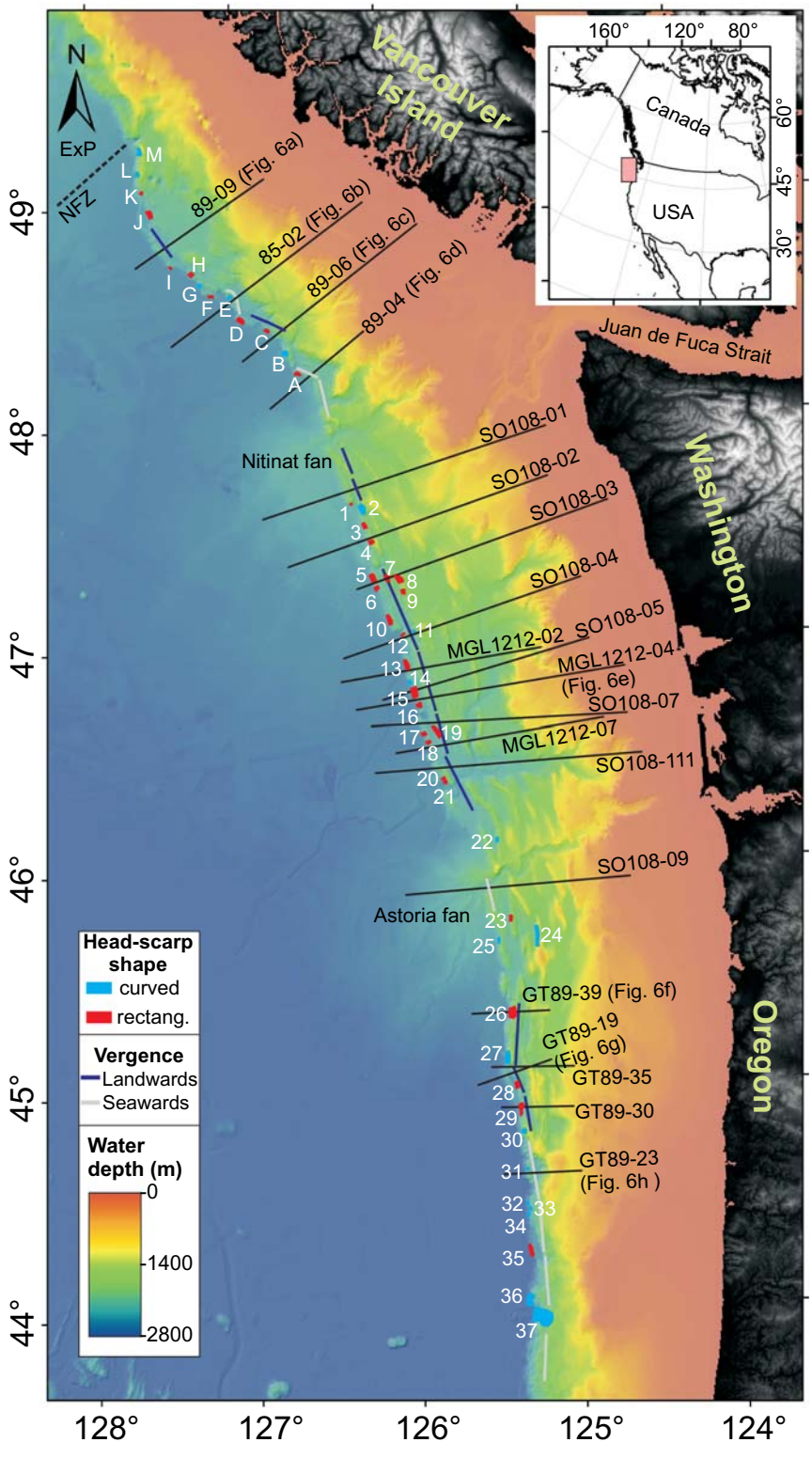

assessing the tsunami hazard associated with slope failures have also been carried out (McAdoo & Watts 2004). However, no comparable study of the tsunami hazard currently exists for slope failures seen along the accretionary prism of northern Cascadia (Scholz 2013).

Here we combine results from previous studies mentioned above using publically available multibeam bathymetric data from the Cascadia margin (44.0–49.5° N) to map and characterize submarine slope failures along the deformation front, and the first three seawards-located thrust ridges of the accretionary prism, where failure geometry is visible on the bathymetry. Thirty-seven failures were mapped off southern Cascadia, which complement the 13 slope failures off northern Cascadia studied by Riedel *et al.* (2016*b*).

We defined several morphological parameters of these 50 failures (e.g. height, azimuth, slope-angle failure area, failure volume) to understand what may control failure style. We intercorrelate these individual parameters and also compare them to the large-scale subduction zone tectonics, as well as along-margin sedimentological settings and gas hydrate occurrences. The results enable us to decipher potential controls on failure style which could be subsequently used to assess risks for tsunami generation.

Geological setting of the Cascadia margin

The Cascadia subduction zone extends from Cape Mendocino, California, to the northern tip of Vancouver Island, British Columbia (Fig. 1). The Juan de Fuca Plate is subducting beneath the North American Plate at a rate of *c.* 45 mm a^{-1} (e.g. DeMets *et al.* 2010). The oceanic plate is relatively young (2–6 Ma at the deformation front: e.g. Atwater 1970; Atwater & Menard 1970), and therefore relatively warm and buoyant (e.g. Davis & Hyndman 1989). The up to 4 km-thick sedimentary section overlying the oceanic plate near the deformation front consists of a mix of fine-grained hemipelagic sediments and coarser-grained turbidites (e.g. Westbrook *et al.* 1994). In contrast to southern Cascadia, sediments off Vancouver Island are generally more coarse grained, and a clear interlayering between glacial and interglacial periods was identified (e.g. Knudson & Hendy 2009; Hamilton *et al.* 2015). At the deformation front, the sedimentary section has been scraped off and accreted to the margin, and along-margin differences in the relative amount of sediment being accreted have been noted (e.g. MacKay *et al.* 1992; Booth-Rea *et al.* 2008). The accretionary prism consists of a series of ridges and folds (Fig. 1). The accretion of sediments is accompanied by overall sediment thickening and deformation, and bulk shortening associated with compaction, as well as fluid expulsion (e.g. Hyndman *et al.* 1993). The upwardly expelled fluids are rich in methane and, as a consequence, gas hydrate occurs across the prism from the deformation front at water depths of *c.* 2200 m to the landwards limit of gas hydrate stability. Several boreholes were drilled off Vancouver Island and Oregon (Northern and Southern Hydrate Ridge) to study gas hydrates (Westbrook *et al.* 1994; Tréhu *et al.* 2003; Riedel *et al.* 2006), which document the gas hydrate environment and associated sedimentology.

The convergent margin of the Cascadia subduction zone has experienced repeated megathrust earthquakes with magnitudes of $M > 8$ (e.g. Rogers 1988; Hyndman & Rogers 2010), believed to be the most significant trigger for submarine slope failures along Cascadia (Scholz *et al.* 2016). Historical evidence for large earthquakes in this region was first documented by Atwater (1987) using sedimentary records of deep-water turbidites. The last megathrust event was determined by Satake *et al.* (1996) to be 26 January 1700, using tsunami records in Japan. The recurrence rate of such large events off Cascadia is estimated to be between 250 and 1000 years (Goldfinger *et al.* 2012).

Data

Data available for our study include legacy data collected with the SEAMARK-II system at the northern Cascadia margin, providing backscatter imagery of the seafloor off Vancouver Island (Davis *et al.* 1987; Davis & Hyndman 1989), and the GLORIA seafloor backscatter imagery for the coasts off Washington and Oregon states (Grim *et al.* 1991). More recently, seafloor multibeam swath bathymetry data were acquired with an EM300 system (Kelley & Delaney 2005). The data are available as a 20 × 20 m first-pass processing grid with acquisition footprint present, and at a lower-resolution 40 × 40 m grid with noise from far-angle beams removed. The

Fig. 1. Bathymetric map of the study region of the Cascadia margin. Slope failures off Vancouver Island are labelled with letters A–M following Riedel *et al.* (2016*b*). Slope failures off Washington and Oregon are labelled as 1–37. Failures with curved head scarps are shown in blue (the same as in Fig. 4), whereas failures with rectangular head scarps are shown in red (the same as in Fig. 4). The locations of seismic lines used for this study are shown by black lines. The dip direction of the first thrust sheet at the deformation front is dark blue if the thrust is landwards vergent, and grey if the thrust is seawards vergent. ExP, Explorer Plate; NFZ, Nootka Fault Zone.

high-resolution grid allowed for a better definition of physical features, despite a visible acquisition footprint, and a higher accuracy in the determination of parameters such as failure volume. For southern Cascadia, seafloor depths were obtained from the multi-resolution bathymetry available online (Ryan *et al.* 2009). This dataset has a varying resolution between 40 × 40 and 50 × 50 m.

Multichannel seismic (MCS) data across the deformation front were collected during several expeditions, which focused on the investigation of the thrust-fault system and the determination of fault vergence (e.g. Hyndman 1995; MacKay 1995; Adam *et al.* 2004; Booth-Rea *et al.* 2008). For the purpose of this study, we use MCS data from the ORWELL expedition (Flueh *et al.* 1998), the COAST project offshore Washington (Holbrook *et al.* 2012), as well as the pre-site survey expedition for ODP Leg 146 (GT89) across Hydrate Ridge offshore Oregon (Moore *et al.* 1995). Data from the MGL1212 and GT89 cruises were accessed using the Academic Seismic Portal at the University of Texas Institute for Geophysics (Christeson *et al.* 2017). No further processing was applied to these datasets. MCS data collected by the Geological Survey of Canada offshore Vancouver Island in 1985 and 1989 (a summary of these surveys is given in Hyndman 1995) were reprocessed with a focus on the frontal ridges. The new processing flow included geometry definition, deconvolution to reduce the bubble-pulse, velocity analysis, stacking and finite-difference time migration. Other seismic data (single-channel streamer, OBS-derived imaging) at northern Cascadia exist and complement the MCS data (Scherwath *et al.* 2006; Lopez *et al.* 2010; Yelisetti *et al.* 2017).

Methodology

Slope failures were identified from the bathymetry using three criteria: (1) visible head scarp; (2) exposed failure plane; and, if possible (3) failed material deposited downslope that has not been completely covered by sedimentation. Numerous additional older slope failures covered by thick sedimentary drape can also be discerned but are not analysed in this study. We only considered failure events that occur on ridges at the deformation front and the first three landwards-located thrust ridges. Several large canyon–fan systems (e.g. Astoria and Nitinat: Fig. 1) disrupt the deformation front, and several plunge-pool features linked to smaller canyon systems exist along the toe of the accretionary prism. These erosional canyons create steep slopes along their paths and cut the prism mostly perpendicular to the orientation of accretionary ridges. Canyon-related slope failures are excluded from our analyses due to complex sediment transport and depositional processes, such as formation of fans and sediment waves. Using the bathymetry, the morphological parameters of ridge azimuth, width, height and the slope angle of the intact ridge, as well as failure plane, failure area, failure volume and scarp shape, were derived for all slope failures. The ridge azimuth (or strike) was measured by determining the direction of slope and adding 90°. For individual failures, ridge azimuths were defined by extracting the aspect values over a selected polygon outside the failed portion of the ridges (Riedel *et al.* 2016*b*) followed by a Gaussian polynomial fit. Ambiguity in ridge orientation due to the symmetry around 360° and 180° was removed prior to defining the average azimuth (see Figs 2 & 3) or was manually measured where bathymetric data quality was poor. The maximum value of the best-fit Gaussian polynomial was used in the following calculations and discussions. An uncertainty of ± 10° was assigned to both the manually defined values and those from the best-fit polynomials. Minimum, maximum and average slope angle for the ridges and failure planes, as well as height (taken at the edge of the head scarp) and width of the ridges, were derived from the bathymetry and individual profiles drawn perpendicular and parallel to the major ridges (Table 1). These values, especially height and width, can vary for each failure along the ridge and average values are reported. Variation in the ridge height can be up to 60 m and the width may vary up to 500 m.

To estimate slope-failure volume, the original shape of the ridge was reconstructed by generating a virtual plane covering the failure scar guided by the shape of the adjacent intact portions of the frontal ridges. The vertical difference between the multibeam bathymetry data and the virtual plane was assumed to represent the failure volume, and zones of net-loss and net-gain were defined in the region of the exposed failure plane. The volume of debris located beyond the toe of a failed ridge was not determined due to the lack of sub-bottom profiler data. Therefore, these volume estimates are only approximate.

Previous studies have subdivided the slope failures off Vancouver Island into two groups according to the shape of their scarp: curved and rectangular (Riedel *et al.* 2016*b*). Using this approach, failures where the headwall and sidewall intersect at 90° ± 5° were classified as rectangular, while those where this was not the case were classified as curved.

In addition to the characteristics of the landslide source area, we also analysed the depositional area by combining multibeam bathymetry and backscatter data. Based on visual analysis, we classified the deposits as ‘blocky’, ‘debris flow’ or ‘indistinguishable’.

Additional information on the direction of compression from borehole breakouts at the northern

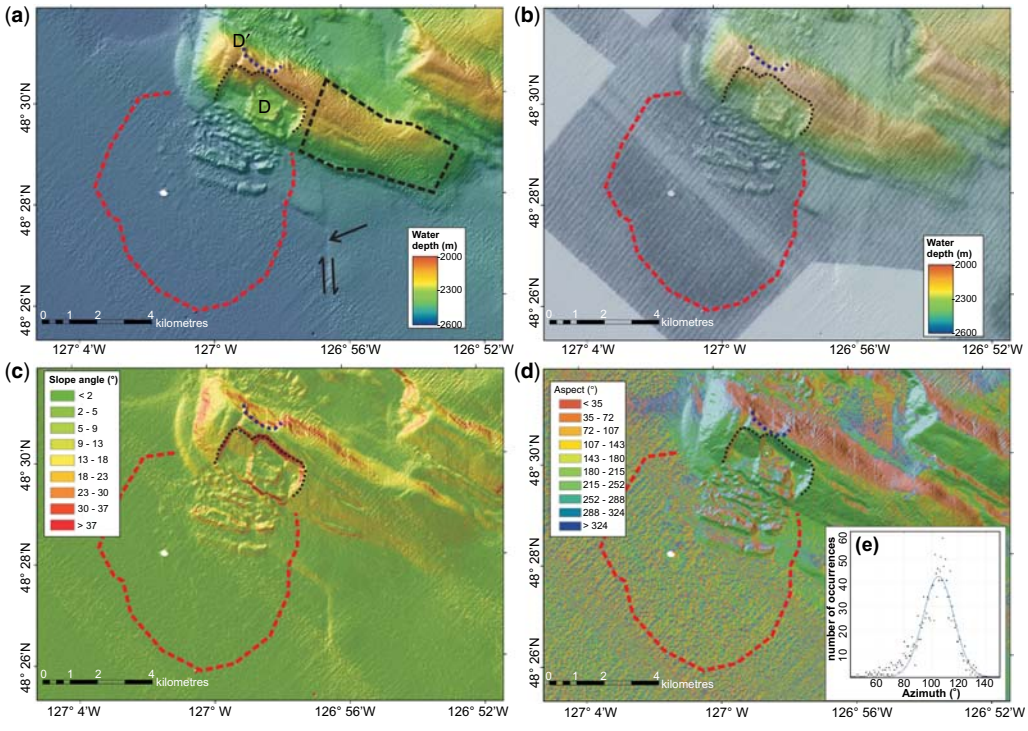

Fig. 2. Details of blocky-style failure D typically associated with rectangular head scarps. (**a**) Colour-shaded bathymetry and relief. Note the prominent strike-slip fault west of the frontal ridge as indicated by black arrows, as well as small failure D′ at the NE flank. (**b**) Superimposed backscatter identifying a large debris field (red dashed line). (**c**) Slope angle derived from bathymetry. The head scarp of failure D is shown as a black dashed line and failure D′ to the NE is outlined by the dashed dark blue line. (**d**) Map of the slope aspect derived from topography. (**e**) Histogram of azimuth values over the selected polygonal region (black dashed line in a) across the intact ridge. A best-fit polynomial fit yields an average azimuth of *c.* 110° for the ridge (Table 1). Multibeam EM300 data in the 20 m × 20 m resolution for the region off Vancouver Island are from Kelley & Delaney (2005).

and the southern Cascadia margin are included. Borehole data from IODP Expedition 311 were used to define the stress regime of the uppermost 300 m of sediments across the prism (Riedel *et al.* 2016*a*). Borehole breakouts have also been used to define such stress orientations at Southern Hydrate Ridge off Oregon (Goldberg & Janik 2006). The maximum horizontal stress that squeezes the borehole and changes its shape is a measure of the overall tectonic forcing around the borehole, and is thus a proxy for the accretionary process, as well as the physical properties (e.g. compressive strength) of the sediments (e.g. Chang *et al.* 2010). Orientations (azimuth of breakout) from five sites of IODP Expedition 311 and from Site 889 of ODP Leg 146 (Riedel *et al.* 2016*a*), as well as three sites at Southern Hydrate Ridge (Goldberg & Janik 2006), were superimposed onto the strike orientations of the bathymetric data to investigate linkages between the stress regime and the surface expressions of sediment accretion.

Results

Morphological analysis of submarine slope failures

A total of 50 slope failures along the deformation front and the first three landwards-located thrust ridges of the accretionary prism were identified over an along-margin distance of 630 km (Fig. 1; Table 1). We established a database containing morphological parameters and information on the stress regime (Table 1). Failure volumes range from 0.04 km^3 in the case of failure I at northern Cascadia to *c.* 11.2 km^3 observed at the southernmost failure (37) off Oregon (Table 1). The majority of failures (*c.* 80%) had volumes of <1 km^3 of sediment removed and failure areas of <10 km^2. Slope angles of the intact ridges varied considerably between 5° and 25°, and the associated height of the ridges ranged from *c.* 300 m to almost 1400 m (above the abyssal plain or adjacent slope basin).

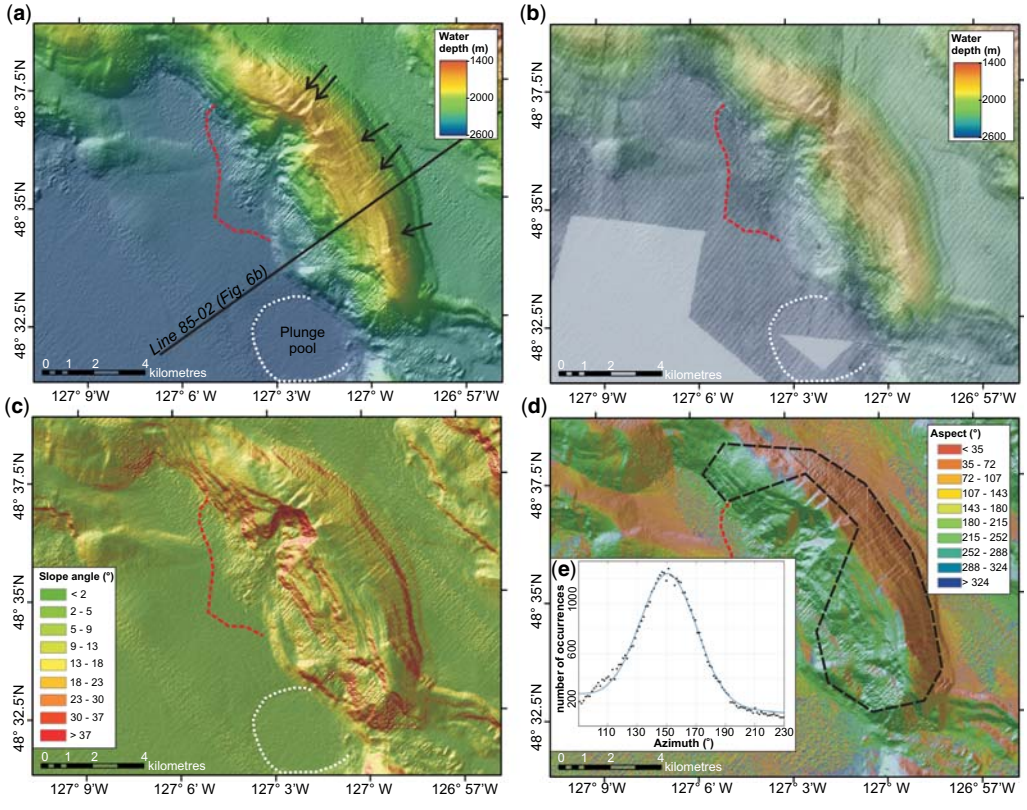

Fig. 3. Details of debris-style failure E typically associated with curved head scarps. (**a**) Colour-shaded bathymetry and relief (note the extensional faults across the ridge; some are depicted by black arrows), and small plunge pool. (**b**) Superimposed backscatter identifying a small debris-field (red dashed line). (**c**) Slope-angle derived from bathymetry. (**d**) Map of the slope aspect derived from topography. (**e**) Histogram of azimuth values from the selected polygonal region (black dashed line) across the intact ridge. A best-fit polynomial fit yields an average azimuth of *c.* 150° for the ridge (Table 1). Multibeam EM300 data in the 20 m × 20 m resolution for the region off Vancouver Island are from Kelley & Delaney (2005).

Thirty-one failures exhibited rectangular head scarps; while 19 failures showed curved head scarps (Table 1). We also noted that rectangular scarps are often associated with intact sediment blocks in the failed mass (22 out of 31 cases); while for curved head scarps, the failed sediments appears (if distinguishable) as an incoherent mass, also referred to as 'debris flow' (only four out of 19 cases). In the following subsection, the prominent slope failures D and E (for the locations see Fig. 1) from the northern Cascadia margin (also analysed by Hamilton *et al.* 2015) are used to demonstrate the methodology for the morphological analysis and to describe the results of the two different failure styles.

Failure D: a blocky-style failure with rectangular head scarp. Failure D, also termed 'Slipstream' (Hamilton *et al.* 2015), is a blocky failure on a ridge *c.* 500 m above the abyssal plain, and is orientated at an average azimuth of *c.* 110° (Fig. 2a; Table 1). The headwall has a rectangular shape, with a failed portion *c.* 3.3 km in width and *c.* 2.0 km in length, covering an area of *c.* 5.0 km^2. High seafloor backscatter (Davis *et al.* 1987) outlines a debris field extending *c.* 4.0 km seawards of the ridge, reaching beyond the extent of the intact deposits (Fig. 2b). Based on the reconstructed shape of the intact ridge, a slope angle prior to failure was estimated to be *c.* 8.4° with a volume of failed material of *c.* 0.22 km^3 (Table 1; Fig. 2c). Ridge orientation is defined with an average azimuth of *c.* 110° (Fig. 2d, e; Table 1). This ridge is also associated with a small failure at the NW-facing slope (denoted failure D′). However, this failure D′ was not included in the statistics as it is the only landwards-facing failure observed and was thus considered atypical. Furthermore, a prominent right-lateral strike-slip fault was seen seawards of the ridge (Fig. 2a). This fault

Table 1. *Geomorphological details of slope failures identified along the frontal ridges of the deformation front*

Latitude	Longitude	Head scarp	Description of failure mass	Ridge height (m)	Ridge width (km)	Failure width (km)	Failure length (km)	Failure area (km^2)	Ridge azimuth (°)	Failure volume (km^3)	Intact ridge slope angle (°)
Northern Cascadia off Vancouver Island											
48° 15.4274′	−126° 36.2151′	R	Blocky	470	2.0	3.3	1.3	4.1	106.2	0.452	14.5
48° 20.5912′	−126° 40.0440′	C	Debris	985	5.0	2.5	2.2	4.6	165.0	0.760	25.0
48° 27.37012′	−126° 47.7217′	R	Blocky	550	1.9	2.4	0.7	1.5	126.0	0.042	12.8
48° 30.4182′	−126° 58.1219′	R	Blocky	500	3.05	3.3	2.0	5.0	109.8	0.222	9.5
48° 36.5702′	−127° 02.0105′	C	Debris	880	4.48	2.0	2.4	2.7	150.1	0.460	16.5
48° 36.8423′	−127° 09.8405′	R	Blocky	370	3.7	2.0	1.2	2.3	100.6	0.128	11.8
48° 39.9053′	−127° 13.9121′	C	Debris	790	3.9	1.8	1.4	2.0	146.7	0.151	21.5
48° 42.8791′	−127° 17.9086′	R	Blocky	540	3.0	2.0	2.0	3.2	126.3	0	11.5
48° 44.9100′	−127° 26.1764′	R	ND	370	2.9	0.8	1.8	1.2	117.6	0.041	9.0
48° 59.4178′	−127° 33.6766′	R	Blocky	450	2.7	1.9	3.4	6.5	154.5	0.332	10.7
49° 05.2859′	−127° 37.0622′	R	Blocky	495	1.8	0.8	1.5	1.0	138.4	0.075	12.8
49° 09.9583′	−127° 38.2454′	C	Blocky	1075	6.0	1.7	2.5	3.9	8.0	0.204	16.0
49° 16.2427′	−127° 37.3566′	C	Blocky	1340	6.2	1.9	3.7	6.4	177.6	0.315	16.0
Southern Cascadia off Washington											
47° 39.9574′	−126° 16.3193′	R	Blocky	550	3.9	1.1	1.4	1.2	95	0.034	16.0
47° 38.5406′	−126° 10.8972′	C	ND	770	3.5	5.2	2.2	7.2	120	1.530	14
47° 33.9005′	−126° 10.4289′	R	Blocky	640	5.0	3.2	2.6	5.4	118.5	0.350	8.2
47° 29.4901′	−126° 07.7149′	R	Blocky	400	4.6	2.5	1.8	4.6	117	0.340	11.3
47° 19.7160′	−126° 7.6154′	R	Blocky	480	3.5	4.4	1.5	5.6	116	0.216	7.1
47° 16.9092′	−126° 06.2140′	R	Blocky	520	5.0	≥2.5	2.2	≥4.5	116	ND	7.1
47° 19.7174′	−126° 02.0680′	R	ND	500	3.0	3.9	1.9	7.8	121	0.574	15.3
47° 19.0717′	−125° 57.0622′	R	ND	300	3.5	≥3.6	≥1.6	≥4.7	121	ND	8.8
47° 15.5654′	−125° 56.2984′	R	ND	500	4.0	≥2.5	1.8	≥4.7	122	ND	14.0
47° 08.4236′	−126° 01.7763′	R	Blocky	550	5.0	5.3	2.0	11.2	113	0.249	11.7
47° 04.7816	−125° 52.6930	C	ND	490	2.5	2.6	1.0	2.04	132.5	0.149	15.6
47° 04.4126′	−125° 57.0224′	R	Blocky	570	4.5	≥1.0	2.4	≥2.4	ND	ND	10.8
46° 55.7153′	−125° 55.76526′	R	Blocky	460	3.2	5.7	2.2	9.9	104	0.554	11.8
46° 51.3529′	−125° 55.0563′	C	Debris	360	3.0	2.5	1.7	3.3	118	0.135	14
46° 48.2896′	−125° 52.7346′	R	Blocky	410	4.0	5.3	3.0	16.4	110.5	0.799	6.7
46° 44.9655′	−125° 51.3470′	R	ND	480	4.5	≥2.7	2.8	≥6.7	110.5	ND	8.5
46° 37.3093′	−125° 50.3810′	R	Blocky	400	4.0	2.1	2.4	4.4	110.5	0.224	7.6
46° 35.0859′	−125° 48.5210′	R	Blocky	400	4.0	1.6	2.2	3.2	110.5	0.291	7.6
46° 37.5447′	−125° 44.5190′	R	ND	280	4.0	6.9	2.3	11.8	119.5	0.931	5.3

(*Continued*)

Table 1. *Geomorphological details of slope failures identified along the frontal ridges of the deformation front* (*Continued*)

Latitude	Longitude	Head scarp	Description of failure mass	Ridge height (m)	Ridge width (km)	Failure width (km)	Failure length (km)	Failure area (km^2)	Ridge azimuth (°)	Failure volume (km^3)	Intact ridge slope angle (°)
46° 25.2316′	−125° 43.3795′	R	ND	650	5.5	1.6	2.1	3.0	126.6	0.086	12.4
46° 24.2481′	−125° 42.7156′	R	ND	650	5.5	1.7	2.1	3.2	126.6	0.163	12.4
Southern Cascadia off Oregon											
46° 07.7794′	−125° 23.7385′	C	ND	550	2.3	1.2	2.6	2.9	175	0.231	17
45° 46.4976′	−125° 19.7192′	R	ND	460	2.5	1.5	3.2	4.3	178	0.103	15
45° 41.5336′	−125° 09.8460′	C	ND	650	3.0	1.8	10.7	17.2	180	2.35	18
45° 40.5298′	−125° 24.7015′	C	ND	500	3.5	0.8	2.9	2.3	180	0.17	14
45° 21.1631′	−125° 20.1691′	R	Blocky	800	4.0	6.2	3.2	16.0	110	2.945	14.0
45° 08.9468′	−125° 22.7109′	C	ND	1000	4.0	6.3	1.7	8.4	185	2.077	18.4
45° 01.7892′	−125° 19.6260′	R	Blocky	600	4.0	≥3.9	2.1	≥7.6	117.5	ND	12.1
44° 55.2502′	−125° 18.5439′	R	Blocky	550	3.0	2.3	6.1	9.8	170	0.8	15.5
44° 49.1206′	−125° 18.1298′	C	ND	900	5.5	2.4	2.0	4.5	175	0.467	16.7
44° 38.9320′	−125° 17.8933′	C	ND	800	5.5	1.6	1.4	1.6	180	0.105	16.7
44° 29.4965′	−125° 18.2323′	C	ND	750	4.0	2.3	1.5	2.4	180	0.282	18
44° 27.8642′	−125° 17.2578′	C	ND	750	4.0	1.8	2.1	2.9	180	0.433	18
44° 26.3342′	−125° 18.1128′	C	ND	750	4.0	1.8	1.4	2.2	180	0.320	18
44° 16.9887′	−125° 17.7060′	R	Blocky	500	4.0	6.5	1.7	8.7	112	0.629	11.5
44° 03.2865′	−125° 18.7020′	C	Blocky	860	ND	2.5	2.5	17.4	196	ND	14
43° 57.5111′	−125° 11.2646′	C	Blocky	1200	ND	7.5	7.6	69.0	196	11.16	11.5

The depositional area of the failure mass is described in general terms for the presence of blocky material more homogenous debris. Where available, data from backscatter or higher resolution 3.5 kHz data were used to aid in the classification.
ND, not defined.
R, rectangular.
C, curved.

does not appear to be displacing the main frontal ridge, only the sediments west of the ridge (as seen by the displacement of a small bathymetric high on the abyssal plain). This fault is part of a series of similar strike-slip faults identified on the abyssal plain (Riedel *et al.* 2016*b*).

Failure E: a debris-style failure with curved head scarp. Slope failure E, also referred to as 'Orca slump' (Hamilton *et al.* 2015), is located at a thrust ridge that rises to *c.* 880 m above the abyssal plane (Fig. 3a). The failure is roughly 2.0 × 2.4 km and covers an area of *c.* 2.7 km^2. High seafloor backscatter from early seafloor imaging (Davis *et al.* 1987) outlines a debris field extending *c.* 4.0 km west beyond the toe of the ridge (Fig. 3b). The slope-angle map (Fig. 3c) defines a minimum slope angle of 12.2° and a maximum of 26.8° for the intact ridge. The estimated volume loss is *c.* 0.47 km^3 (Table 1). The ridge is orientated at an average azimuth of *c.* 150° (Fig. 3d, e; Table 1). This ridge is characterized by numerous extensional faults (Scherwath *et al.* 2006; Lopez *et al.* 2010), developed mostly from the top to the landwards-facing flank of the ridge (Fig. 3a). The headwall has a curved shape following the general shape of the ridge (Fig. 3d).

General correlations between morphological parameters of ridges and failures

Using the parameters derived from the bathymetric data for the 50 slope failures and the associated ridges (Tables 1 & 2), cross-plots were generated to determine possible inter-relationships between the parameters. From these distributions, it can be seen that the failures with curved head scarps (and predominantly debris-flow deposits) occur mostly at ridges with higher elevations above the abyssal plain (or adjacent basin) and slopes at an angle of more than *c.* 14°. Ridges showing rectangular head scarps (and predominant blocky-style failure) occur on ridges of lower height (with one exception, all are <650 m) and slope angles of less than 16° (Fig. 4a). Curved head scarps and debris-style failures occur at ridges with azimuths above *c.* 150°. South of failures 36 and 37 (*c.* 44° N), a significant change in the shape of the deformation front and the accretionary prism can be seen (Fig. 1). Further south there are no clearly defined ridges and the entire deformation front shows evidence of slope failures, and many intact blocks of varying sizes are seen seawards of the deformation front. In that sense, slope failures 36 and 37 are already atypical (and were excluded from correlations) to observations made along the deformation front northwards to off northern Vancouver Island.

Blocky-style failures are linked to ridges with rectangular head scarps but occur at ridges with a wide range of azimuths considering the entire margin; whereas off Vancouver Island, they are at an average azimuth of *c.* 120° (Fig. 4b). The data visualized in Figure 4 show overall no correlation between the various geometrical parameters of ridges associated with rectangular head scarps and blocky-style failure masses.

Correlation of failure styles to subduction zone parameters

Ridge geometries. The seafloor of the accretionary prism of the Cascadia margin exhibits a pattern of individual small ridges along the deformation front. The frontal ridge system is broken into short, 5–15 km segments at distinct (and systematically changing) azimuths (Fig. 5). Off northern Cascadia, the prism thrust ridges show a dominant azimuth of 110°–120°, with a range from 95° to 175° (Fig. 5a). A small subset of ridge segments follows an azimuth of *c.* 30°. Ridges at the deformation front, which are predominantly along an azimuth of *c.* 120°, show blocky-style failures with rectangular head scarps. Fewer ridges are along an azimuth of *c.* 160°, but these show predominantly debris-style failures and curved head scarps. Overall, the stress orientation, as indicated by borehole breakouts at most sites analysed by Riedel *et al.* (2016*a*), align to ridges with an azimuth of *c.* 120°. However, the subduction direction of *c.* 45° (DeMets *et al.* 2010) is markedly different from the dominant ridge orientation.

At southern Cascadia there is a narrower spread of ridge azimuths (Fig. 5b), which are also rotated by *c.* 40° relative to ridges at northern Cascadia. Borehole breakouts determined at three sites at Southern Hydrate Ridge (Goldberg & Janik 2006) are not correlated to the overall ridge orientation. However, the direction of compression measured from Site 1445 is parallel to the subduction direction (DeMets *et al.* 2010). The two styles of slope failure appear to occur at either end of the spectrum of ridge orientations: failures with curved head scarps are observed at ridges with an almost north–south orientation (180°); whereas blocky-style failures with rectangular head scarps are occurring at ridges with an azimuth of *c.* 150°.

Fault vergence. To image the deformation front thrusts offshore Vancouver Island, regional MCS data were acquired in 1985, as well as part of the Lithoprobe project (Hyndman 1995). Low frequencies (<40 Hz) of the airgun array (with a volume of *c.* 6000 inch^3) and offsets of up to 3800 m allowed imaging to the top of the oceanic crust while preserving structural resolution within the accretionary prism. Representative transects across the deformation front are shown in Figure 6, where ridges have

Table 2. *Comparison of the vergence structure of ridges and the failure style*

Name	Failure style	Head scarp	Length of segment (km)		Length ratio a/b	Seismic-based thrust vergence
			a	*b*		
Northern Cascadia off Vancouver Island						
A	Blocky	R	1.4	2.0	0.7	Sea Line 89-04*
B	Debris	C	3.0	2.0	1.5	
C	Blocky	R	2.0	0.8	2.5	
D Slipstream	Blocky	R	2.1	1.0	2.1	Land Line 89-06*
E Orca	Debris	C	3.0	2.0	1.5	Sea Line 85-02*
F	Blocky	R	2.2	0.8	2.8	
G	Debris	C	2.0	1.0	2.0	
H	Blocky	R	2.5	0.8	3.1	
I	ND	R	2.8	1.2	2.3	Land Line 89-09*
J	Blocky	R	1.6	0.3	5.3	
K	Blocky	R	1.6	0.5	3.2	
L	Blocky	C	1.4	0.8	1.8	
M	Blocky	C	2.2	1.2	1.8	
Southern Cascadia margin off Washington						
1	Blocky	R	2.0	1.5	1.3	
2	ND	C	ND	ND	ND	
3	Blocky	R	4.2	1.0	4.2	
4	Blocky	R	3.5	1.5	2.3	
5	Blocky	R	3.0	0.6	5.0	Land Line SO108-103†
6	Blocky	R	3.5	0.8	4.4	
7	ND	R	2.2	1.2	1.8	
8	ND	R	2.5	2.0	1.25	
9	ND	R	2.0	2.0	1.0	
10	Blocky	R	2.8	0.4	7.0	
11	ND	C	2.0	0.5	4.0	Land Line SO108-104†
12	Blocky	R	3.0	1.0	3.0	
13	Blocky	R	2.4	1.0	2.4	Land MGL1212 Line 02‡
14	Debris	C	2.0	1.0	2.0	
15	Blocky	R	4.0	0.5	8.0	Land MGL1212 Line 04‡ Line SO108-105§
16	ND	R	4.5	0.6	7.5	
17	Blocky	R	4.0	1.2	3.3	Land Line SO108-107†
18	Blocky	R	3.0	0.8	3.8	Land MGL1212 Line 07‡
19	ND	R	2.5	0.8	3.1	
20	ND	R	3.5	1.5	2.3	
21	ND	R	3.5	1.5	2.3	
Southern Cascadia off Oregon						
22	ND	C	1.8	1.5	1.2	Sea Line SO108-109†
23	ND	R	1.8	3.0	0.6	Sea Line SO108-109†
24	ND	C	2.0	1.0	2.0	
25	ND	C	2.5	1.5	1.7	
26	Blocky	R	4.5	1.5	3.0	Land GT8909 Line 39§
27	ND	C	3.2	1.8	1.8	Sea GT8909 Line 35§
28	Blocky	R	2.8	0.9	3.1	Land GT8909 Line 19§
29	Blocky	R	2.5	1.0	2.5	Land GT8909 Line 30§
30	ND	C	3.0	a.l. 2.0	<1.5	Land GT8909 Line 44§
31	ND	C	3.4	a.l. 2.0	<1.7	Sea GT8909 Line 23§
32	ND	C	1.8	0.9	2.0	
33	ND	C	ND	ND	ND	
34	ND	C	2.0	1.0	2.0	

(*Continued*)

Table 2. (*Continued*)

Name	Failure style	Head scarp	Length of segment (km)		Length ratio a/b	Seismic-based thrust vergence
			a	*b*		
35	Blocky	R	2.5	1.5	1.7	
36	Blocky	C	ND	ND	ND	
37	Blocky	C	ND	ND	ND	

a.l., at least; ND, not defined.
*Hyndman (1995, Fig. 6).
†Sonne Expedition SO108 (Flueh *et al.* 1998).
‡Cruise MGL1212 COAST project (Holbrook *et al.* 2012).
§GT89-9 (Moore *et al.* 2015).

not failed to highlight the change in vergence of the underlying thrusts and complexities of sediment deformation.

The northernmost example of line 89-09 (Fig. 6a), representative of failures H and I (blocky failure and rectangular head scarp), depicts a complex mix of landwards- and seawards-vergent thrust faults. However, the dominant structure appears to be landwards vergent, as the minor seawards-vergent faults are truncated at a sedimentary layer buried about 1 s two-way time (TWT) (*c.* 1.2 km depth) below the seafloor. This complex structure appears to indicate different times of fault motion, with an initial (and possibly still ongoing) motion along the seawards-vergent thrust but subsequent overprinting by additional compression giving rise to the landwards-vergent set of faults. There is some evidence of the presence of seawards-verging proto-thrusts within the package of incoming sediments on top of the oceanic plate.

Near the ridge with slope failure E (curved head scarp and debris flow), line 85-02 shows a mix of both landwards- and seawards-verging thrusts (Fig. 6b), but no proto-thrust is seen. Within the centre of the frontal ridge, sediments are strongly folded and seismic reflectivity of these layers is reduced due to the steep dip of the layers. In contrast, the main seawards-verging thrust sheet is clearly imaged, at which underlying sediment are sharply truncated. Displacements along this thrust sheet exceed 2 km. A landwards-vergent back-thrust is indicated by the dip of the sediments, but is poorly imaged by the seismic data.

The next line located to the south (line 89-06) shows a different structure, where the frontal ridge (representative of failures C and D) is underlain by a steeply dipping landwards-verging thrust (Fig. 6c). A seawards-verging proto-thrust, *c.* 6 km west of the frontal ridge, has developed but is covered (draped) by up to 140 m of sediment without any visible fault offset.

Line 89-04 is located near slope failure A (Fig. 6d). Here, a stack of seawards-vergent thrust sheets developed associated with gentle folding of the sediments. Small sediment-filled basins landwards of the thrust sheets have formed, in part structurally deformed (Fig. 6d). This region shows a prominent change in the ridge azimuth (Fig. 1) without a change in the thrust-sheet vergence.

Numerous MCS data off southern Cascadia that image down to the top of the oceanic crust are available from a number of expeditions. The first MCS line south of the Juan de Fuca Strait off Washington is line SO108-101. Here, the frontal ridges show landwards-verging thrusts (Flueh *et al.* 1998). All seismic data located southwards of the Astoria fan also show dominantly landwards-vergent frontal thrust faults (Fig. 6e–g). A change to seawards-vergent thrusts is seen south of 45°15′ N, especially around the deformation front near Hydrate Ridge, described by Moore *et al.* (1995) and MacKay (1995). MCS Line GT89-23 demonstrates the seawards-verging main thrust and landwards-vergent back-thrust along this portion of the margin (Fig. 6h). The region around Hydrate Ridge is characterized by numerous small failures, all with curved head scarps. South of Hydrate Ridge, the failure style is again dominantly blocky with rectangular head scars; yet, fault vergence remains dominantly seawards. Only two examples were chosen from this region, including the largest failure of all, Failure 31, with a volume of *c.* 11 km^3 (Table 1), as many of the smaller (in part, overlapping) events are not discernible from each other and are close to the resolution limit of the data (*c.* 40 × 40 m grid).

Discussion

The combination of (1) morphological parameters for the slope failures and associated thrust-ridges (e.g. slope angle, volume, area: Fig. 4; Table 1),

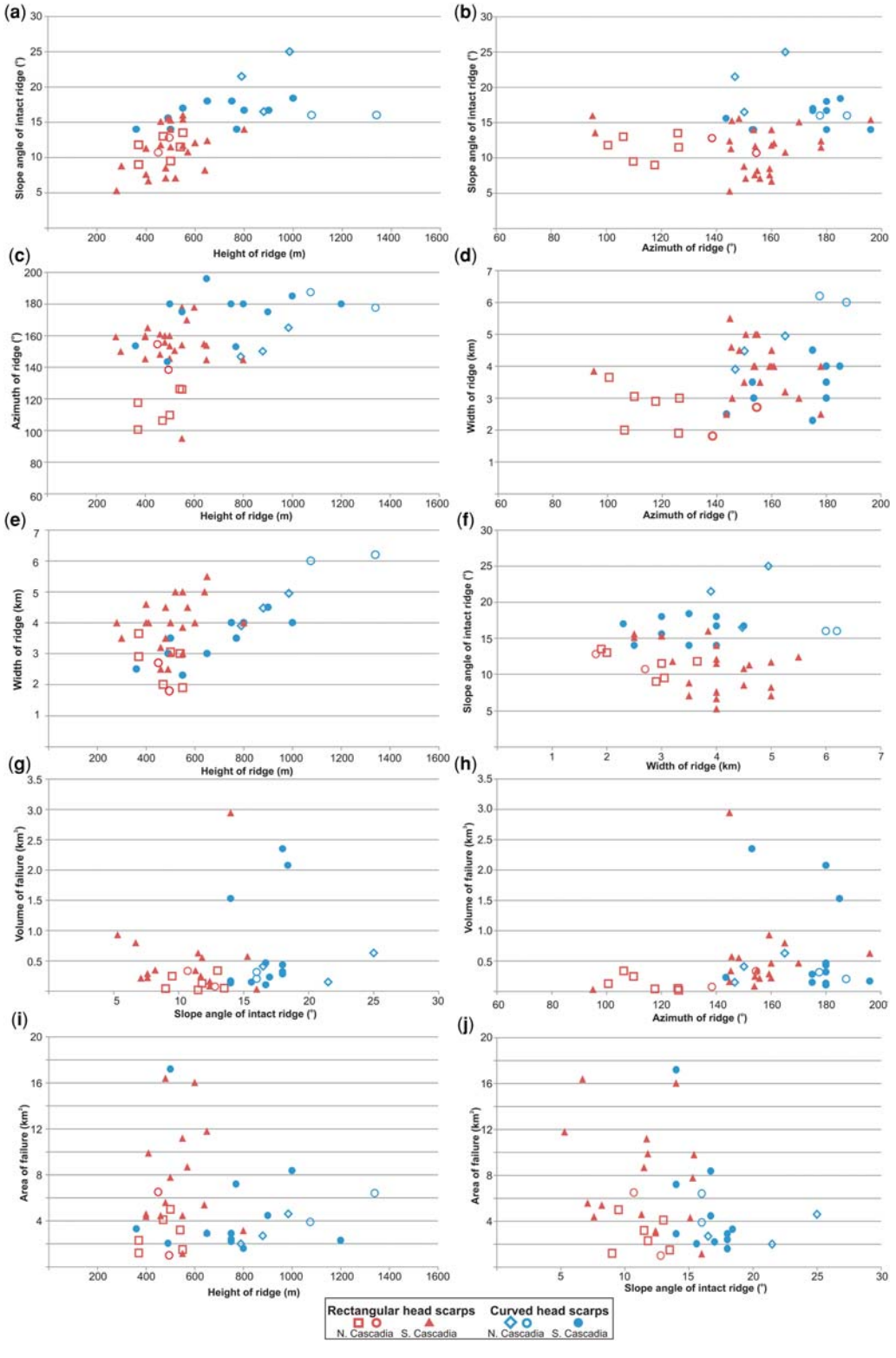

with (2) structural and tectonic parameters (e.g. fault vergence, ridge azimuth: Figs 5 & 6; Tables 1 & 2) does not reveal a distinct pattern of head-scarp occurrence (cf. Fig. 1) or correlation regarding their location along the Cascadia margin. However, a few significant similarities in the observations, parameter dependencies and correlations emerge from the available datasets and analyses, which may help to determine underlying controls on failure style and occurrence:

- Blocky-style failures that are predominantly linked to rectangular head scarps occur on ridges with different azimuths to debris-style failure predominantly linked to curved head scarps, despite evident differences and a clockwise rotation of azimuths between northern and southern Cascadia.
- Curved head scarps and their dominantly associated debris-style failures occur on ridges that are higher and steeper than ridges hosting blocky-style failure with rectangular head scarps.
- Failure volume is uncorrelated to failure style or head-scarp geometry.
- Failure style and head-scarp geometry are uncorrelated to the vergence of the frontal thrust sheet.
- A prominent zig-zag pattern and segmentation of the deformation front off Vancouver Island is identified (Figs 1 & 5). Further south off Washington and Oregon, the zig-zag pattern is less pronounced, and ridges are more closely aligned in a coast-parallel sense. Frontal ridges off Vancouver Island are along an average azimuth of *c.* 120°, with a few ridges at *c.* 150° with two different forms of slope failure recognized, which occur on similar orientated segments along the deformation front.

A simple relationship considering the structure and morphology of an associated thrust-ridge was developed to explain the occurrence of the two main failures types shown in Figure 4: failures initiated at taller ridges have a higher potential energy and can thus generate the higher kinetic energy during failure that is required to cause debris-style mixing of the sediment. In contrast, there is less potential energy at smaller, more gently sloped ridges, which results in failures with intact sediment blocks.

Reasons for these differences in height and the steepness of the intact ridges possibly relate to the nature of the underlying thrust-fault system. High ridge elevation may be the result of stronger thrust forces and/or a longer time to accumulate uplift. Faster and/or longer times of uplift could create larger rates of horizontal compression and thus higher amounts of pore-fluid advection and overpressure. Elevated pore pressures can lead to ridge failure, while the increase in ridge height leads to the appearance of extensional faults (perpendicular to the ridge axis) due to low internal cohesion, thus resulting predominantly in curved head scarps and debris-style failure.

Vergence of the underlying thrust faults was defined from seismic data and using results from previous studies by Flueh *et al.* (1998), Adam *et al.* (2004) and Booth-Rea *et al.* (2008), as well as the neo-tectonic map available for offshore Oregon (Goldfinger *et al.* 1992). In general, the ridges are asymmetric with gentle western-facing and steeper eastern-facing flanks. The opposite pattern is observed at slope failure A off Vancouver Island, and along a segment off Oregon, close to Hydrate Ridge (e.g. Cochrane *et al.* 1994; MacKay 1995; Moore *et al.* 1995). If the main thrust is dominantly landwards vergent, the ridge flank is steeper and shorter on its landwards side (Table 2; Fig. 7a) than if the thrust is seawards vergent (Fig. 7b). Landwards-vergent thrusts produce gentler sloping ridge flanks towards the west (seawards), where most slope failures are observed. There is no clear correlation between thrust-fault vergence and the style of failure. However, debris-style failures with curved head scarps only occur if a landwards-vergent back-thrust exists in combination with a seawards-vergent main thrust, as seen at slope failure E (Orca) (Fig. 6b), or failures 23 and 26–29 off Oregon (Fig. 6h), respectively. The combination of these two fault systems creates a pop-up structure (Fig. 7c) that ultimately leads to the oversteepening of the ridge, its collapse and the formation of extensional faults.

Origin of dual vergence and ridge oversteepening, and associated azimuthal changes

Thrust faulting at different azimuths relative to the overall convergence rate could be the result of a number of factors including: (1) differential forces in response to the main slab-pull; (2) orientation of the overriding plate and backstop (using the coastline

Fig. 4. Cross-plots of physiographical data from the intact ridge systems that host slope failures. (**a**) Height of ridge v. slope angle. (**b**) Azimuth v. slope angle. (**c**) Height v. azimuth. (**d**) Azimuth v. width. (**e**) Height v. width. (**f**) Width v. slope angle. (**g**) Slope angle v. failure volume. (**h**) Azimuth v. Failure volume. (**i**) Height v. area of failure plane. (**j**) Slope angle v. area of failure plane. Ridges near the Nootka Fault Zone and the Explorer Plate, north of the plate rotation point introduced in Riedel *et al.* (2016*b*) are shown by open circles.

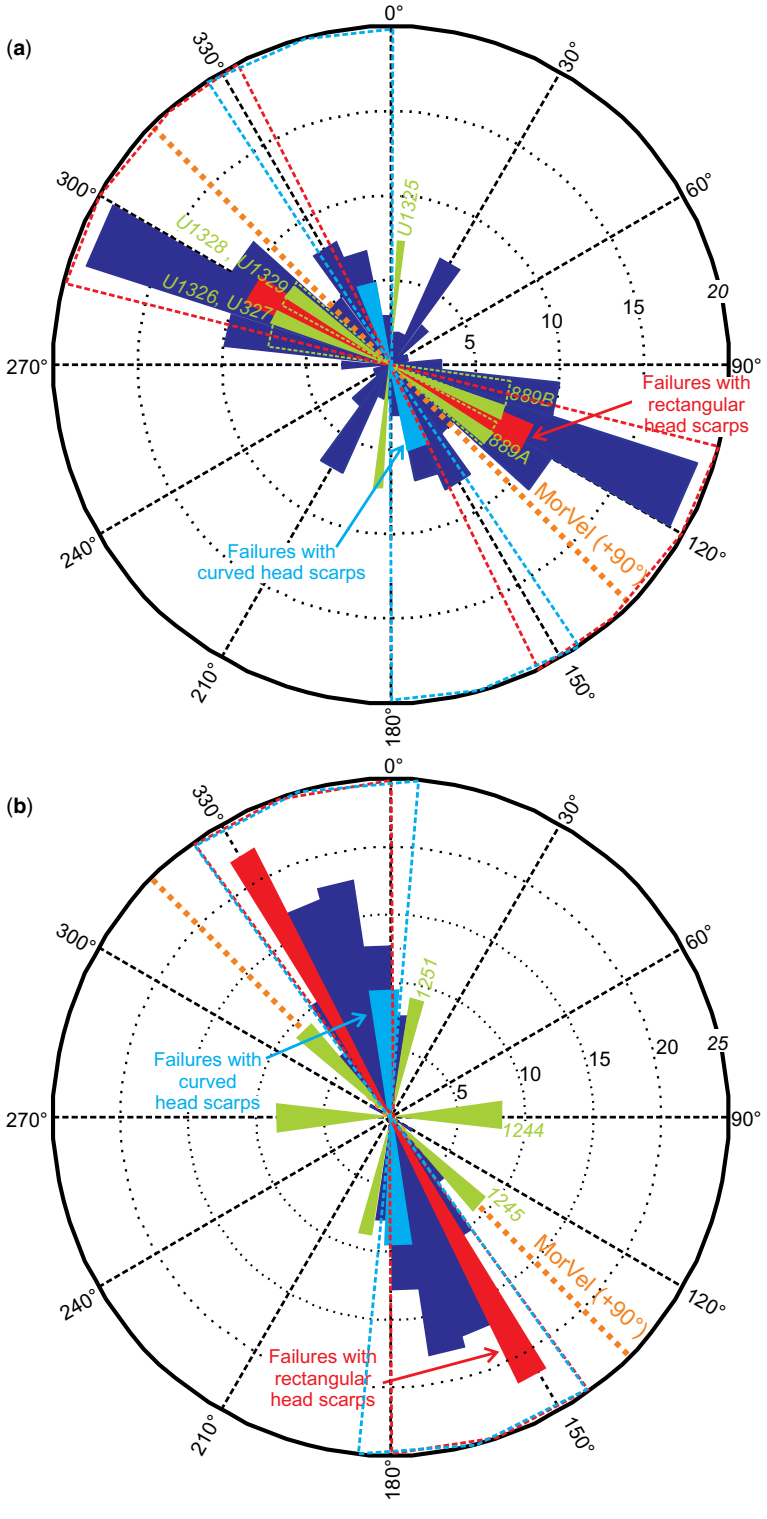

and/or emplaced accreted terranes as guidance); (3) possible palaeo-reorientation of the overall subduction direction; or (4) complex interactions of active faults on the incoming oceanic plate that may break the slab up into smaller segments. It has been noted that several apparent strike-slip faults (orientated nearly north–south at *c.* 175°) are present west of the deformation front off Vancouver Island (Fig. 2), but no clear transform faults have been seen within the accretionary prism. In contrast, the prism off Washington and Oregon is characterized by several transform faults (e.g. Goldfinger *et al.* 1996, 1997) associated with clockwise block rotation of the entire prism (e.g. Goldfinger *et al.* 2000). The prominent zig-zag segmentation of the deformation front off Vancouver Island with two dominant ridge azimuths is proposed to be the result of two main acting forces related to the orientation of the backstop: a dominant ridge azimuth of *c.* 120° represents the portion of the deformation front parallel to the coastline of Vancouver Island; whereas the dominant ridge azimuth of *c.* 150° is linked to segments of the deformation front which are parallel to the coastline off Washington. The distance between individual segments may be governed by pre-existing planes of weakness within the oceanic plate which are represented by the strike-slip faults west of the deformation front. However, processes related to prism fragmentation and block rotation from oblique subduction, as demonstrated by Goldfinger *et al.* (1996, 1997), may also be possible causes for the observed pattern.

In addition to the subduction-related tectonic parameters, there may be other factors controlling the observed differences in the style of failure. In the following section, we discuss several parameters that are often linked to different styles of submarine landslides: (i) sediment type (e.g. Sawyer *et al.* 2012); (ii) gas hydrates (e.g. Sultan *et al.* 2004); and (iii) earthquake shaking patterns (e.g. ten Brink *et al.* 2009).

(i) Differences in sediment type. Sedimentation along the Cascadia margin varies, and deposits include predominantly pelagic/hemipelagic muds and coarser-grained turbidite layers as defined from ODP and IODP drilling (Westbrook *et al.* 1994; Tréhu *et al.* 2003; Riedel *et al.* 2006). The sedimentation pattern differs between glacial and interglacial periods, and the interface between these two types of sediments can easily be seen in sediment cores (e.g. Hamilton *et al.* 2015). At the end of each glaciation cycle, sedimentation rates were higher and sediments from deglacial deposits were often fine-grained silt or silty mud (Hamilton *et al.* 2015). However, as the maximum extent of Quaternary glaciation along the west coast extended to the present-day Juan de Fuca Strait (e.g. Booth *et al.* 2003), sediments off Washington and Oregon may be less influenced by ice-rafted debris. However, the two large systems of the Nitinat and Astoria fan deposited thick sequences of sediment onto the margin and adjacent abyssal plain, thereby impacting the overall sediment properties and associated prism mechanics (e.g. Adam *et al.* 2004).

A general north to south decrease in the volume of sand may be present across the Cascadia accretionary prism extending from off Vancouver Island to off Washington and Oregon, as proposed by Riedel *et al.* (2010). Canyon systems also form characteristic depositional depressions at the toe of the accretionary prism (plunge pools) and occasionally larger sediment-wave features extending for up to 20 km across the abyssal plain. Although sediment transport downslope from canyons and subsequent deposition on the abyssal plain is likely to be associated with a gradual sorting of sediment, the deposition always bypasses those ridges showing slope failures.

While large-scale changes in sediment deposition rates, grain size and composition exist along the Cascadia margin and thus may influence sediment strength, there is no systematic change in failure style relative to the location of canyons, fans or the maximum extent of the ice sheet during the last glacial maximum. Therefore, we rule out changes in sediment composition as the cause of the different slope-failure styles.

(ii) Different distribution of gas hydrate saturation. Gas hydrates within sediments affect the overall sediment stiffness. Higher gas hydrate saturations

Fig. 5. Rose diagram of azimuths (radius is the number of occurrences) of digitized prism-wide lineaments. (**a**) At the northern Cascadia margin off Vancouver Island (Riedel *et al.* 2016*b*). (**b**) At the southern Cascadia margin off Washington and Oregon. A distinction between lineaments from ridges with rectangular head scarps (and predominantly blocky failures) (red bars) v. those from ridges with failures showing curved head scarps (and often debris-flows) (blue bars) is made. The average azimuth is plotted in filled bars (width is equal to the average standard deviation) and the entire range in observed values (see Table 1) is indicated by dashed outline open bars. Superimposed is the orientation of the subduction-related compression rotated by +90° to represent the strike orientation of the Mid-Ocean Ridge Velocity (MorVel) vector (orange dotted line) for off central Vancouver Island. Also shown are azimuths of borehole breakouts at (a) northern Cascadia from IODP Expedition 311 (green bar: sites U1325–U1329) and ODP Leg 146 (dashed green bar: Site 889A, B) (Riedel *et al.* 2016*a*) and (b) southern Cascadia at Hydrate Ridge from ODP Leg 204 (green bar: sites 1244, 1245 and 1251) (Goldberg & Janik 2006).

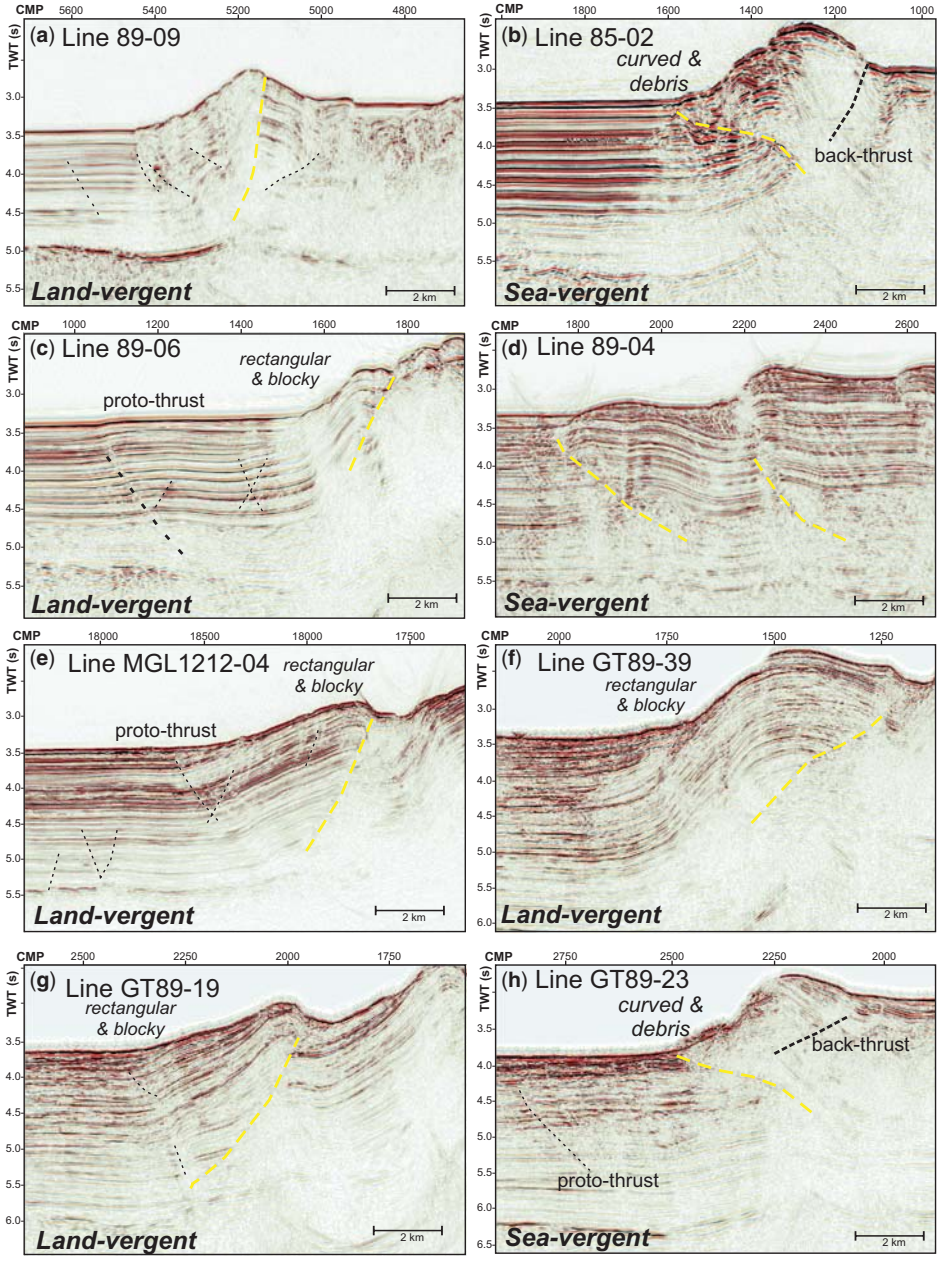

Fig. 6. Examples of seismic sections (plotted at the same horizontal and vertical scale) along the Cascadia margin (for the location see Fig. 1) highlighting changes in the vergence of frontal deformation ridges and thrusts. (**a**) Northernmost line 89-09 (between failures I and J) showing a dominant landwards-vergent thrust, with an overprint of seawards-vergent thrusts that do not completely penetrate the sediment sequence on top of the oceanic plate. **(b)** Line 85-02 (near failure E) with a seawards-vergent main thrust and a landwards-verging back-thrust. (**c**) Line 89-06 (representative of ridges with slope failures C and D) with a dominantly landwards-vergent thrust and the development of a seawards-vergent proto-thrust. (**d**) Line 89-04 near slope failure A depicting solely seawards-vergent thrusts. (**e**) Line MGL1212-04 with a dominantly landwards-vergent thrust off Washington near failure 15. (**f**) Line GT89-39 near failure 26 with landwards-vergent thrust. (**g**) Line GT89-19 at failure 27 with landwards-vergent thrust. (**h**) Line GT89-23 representative of seawards-vergent thrust with a landwards-vergent back-thrust at failures 31–34. CMP, common mid-point; TWT, two-way travel time.

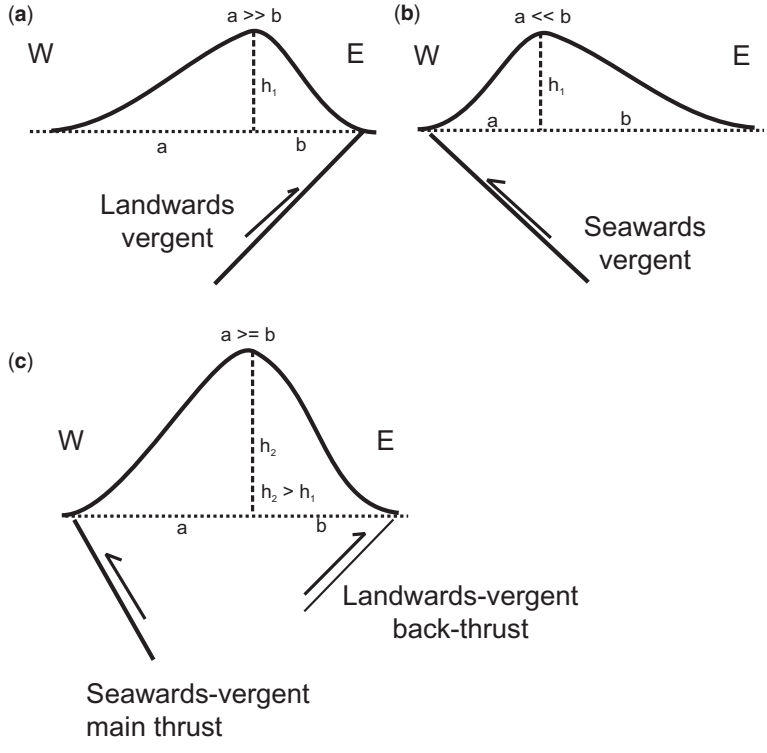

Fig. 7. Sketches depicting the definition of (**a**) landward-vergence and (**b**) seawards-vergence of thrust sheet and associated shape of the frontal ridges. The length of ridge segments *a* and *b*, defined at the maximum elevation of the ridge (*h*), are reported for all slope failures in Table 2. (**c**) Sketch of ridges with a combination of a seawards-verging main thrust with a landwards-verging back-thrust oversteepening the ridge, resulting in debris-style failures, curved head scarps and extensional faulting.

may also create a cementing effect. Gas hydrate saturation within subseafloor sediments were determined in detail: for example, at Northern and Southern Hydrate Ridge based on data from ODP legs 146 and 204 (e.g. Tréhu *et al.* 2004), and along the northern Cascadia margin, using ODP Leg 146 (e.g. Yuan *et al.* 1996, 1999) and IODP Expedition 311 data (e.g. Chen *et al.* 2008; Lopez *et al.* 2010). Analyses of the correlation between sediment type and hydrate morphology and concentration show that gas hydrates at the northern Cascadia margin occur predominantly as pore-filling material in the turbidite sands (e.g. Torres *et al.* 2008; Riedel *et al.* 2010). In contrast, gas hydrates occur more often in the form of a grain-displacing material (nodules or veins) at Hydrate Ridge off Oregon (Tréhu *et al.* 2003). These differences in hydrate morphology and sediment type have previously been attributed to the regional (north–south) decrease in the amount of sand along the Cascadia margin (Riedel *et al.* 2010). While there appears to be regional variations in gas hydrate occurrences, there is no similar north–south trend in failure style.

Seismic and borehole data were used to delineate gas hydrate distributions across the two adjacent frontal ridges with failures D (blocky style) and E (debris style). At the ridge hosting failure E, a layer at 100–140 m with high velocity of up to 2200 m s^{-1} has been identified by drilling and logging (Riedel *et al.* 2006) and from seismic data (Lopez *et al.* 2010). A similar high-velocity layer was defined at the ridge hosting failure D by Yelisetti *et al.* (2014) using the same seismic techniques. Both ridges, very different in their morphological characteristics, do not show a significant difference in gas hydrate saturation. Using this local comparison, as well as the margin-wide change in gas hydrate occurrence, we eliminate changes in gas hydrates saturation or morphology as a factor contributing to the change in slope failure style. Yet, gas hydrate dissociation could yield local overpressure generation and thus potentially stimulate failure, as discussed, for example, by Scholz *et al.* (2016).

(iii) Earthquake shaking pattern relative to ridge azimuth. Large megathrust earthquakes are suspected to

be a major trigger for slope failures along this margin (e.g. Scholz *et al.* 2016). Megathrust earthquakes have involved the entire Cascadia margin (e.g. Satake *et al.* 2003) and shaking patterns for each thrust event are possibly quite similar. The orientation of the ridges relative to the direction of shaking may result in different resonance behaviour of the ridges, similar to those in sedimentary basins (e.g. Rial *et al.* 1992; Semblat *et al.* 2005) and as shown by Bouchon (1973). Segments orientated at one azimuth may experience amplification of shaking and, in contrast, a ridge system at a different azimuth may experience relative damping or less forcing. In this current study, we do not model the soil response expected during a megathrust event because the required parameters, such as sediment shear properties, are unavailable. The distance of the frontal ridges to the updip limit of a megathrust earthquake are relatively short (only few kilometres) and the radiation pattern of shaking induced by such a large earthquake would not be likely to change drastically over the short distances between ridge segments of different azimuths. As such, the quickly changing ridge segments (of the order of *c.* 10 km) may all be within the same lobe of shaking pattern, and therefore we discount different amplification patterns as a cause for the different styles of slope failure.

Conclusion

Slope failures along the deformation front of the Cascadia margin show a systematically changing pattern. The shape of the source areas can be divided into rectangular and curved head scarps. The deposits of rectangular head scarps consist in most cases of blocky material, and occur on ridges with slope angles less than 16° and ridge heights less than *c.* 650 m. The incoherent (debris-flow) mass movements predominantly linked to curved head scarps are mostly associated with taller (>650 m) and steeper (>14°) ridges. The failure mode is linked to ridge azimuth along the northern Cascadia margin. A simple explanation involves the differences in kinetic energies of the failure process between higher ridges (that also are steeper) and smaller (more gently sloping) ridges. During failure, the former possess a higher kinetic energy, which enables a more extensive internal destruction of the failing sediment mass. In contrast, the lower kinetic energy of the more gently sloping, smaller ridges leaves sediment blocks intact.

The pattern in slope failure along the Cascadia subduction zone is likely to be the result of complex tectonic forces along the margin. In cases where a ridge is underlain by a seawards-vergent thrust as well as a landwards-vergent back-thrust, the combined tectonic forces create tall and steep ridges. If a back-thrust does not occur, then both seawards- and landwards-vergent thrusts create smaller ridges. Thus, the type of underlying fault-system may control the failure style. Where two thrust faults lead to the oversteepening of the ridges, they might also support the generation of overpressure and increased fluid flow due to faster compression and porosity reduction. This can add to the preconditioning of the slopes to failure and lead to ridge collapse, as supported by the observation of numerous extensional faults along the ridge crests.

Acknowledgements Data used in this study stem from numerous previous expeditions to the Cascadia margin. We would like to thank all scientists and crew involved in data acquisition and processing. Additional thanks go to Roger McLeod (GSC-Pacific) for providing geo-referenced imagery of the SEAMARK-II data and Robert Kung (GSC-Pacific) for providing legacy ArcGIS datasets off Vancouver Island. We also thank two anonymous reviewers for their detailed comments and suggestions.

Funding This research received no specific grant from any funding agency in the public, commercial or not-for-profit sectors.

References

Adam, J., Klaeschen, D., Kukowski, N. & Flueh, E. 2004. Upward delamination of Cascadia Basin sediment infill with landward frontal accretion thrusting caused by rapid glacial age material flux. *Tectonics*, **23**, TC3009, https://doi.org/10.1029/2002TC001475

Atwater, B.F. 1987. Evidence for great Holocene earthquakes along the outer coast of Washington State. *Science*, **236**, 942–944.

Atwater, T. 1970. Implications of plate tectonics for the Cenozoic tectonic evolution of western North America. *Geological Society of America Bulletin*, **81**, 3513–3536.

Atwater, T. & Menard, H.W. 1970. Magnetic lineations in the northeast Pacific. *Earth and Planetary Science Letters*, **7**, 445–450.

Booth, D.B., Troost, K.G., Clague, J.J. & Waitt, R.B. 2003. The Cordilleran ice sheet. *Development in Quaternary Science*, **1**, 17–43.

Booth-Rea, G., Klaeschen, D., Grevemeyer, I. & Reston, T. 2008. Heterogeneous deformation in the Cascadia convergent margin and its relation to thermal gradient (Washington, NW USA). *Tectonics*, **27**, TC4005, https://doi.org/10.1029/2007TC002209

Bouchon, M. 1973. Effects of topography on surface motion. *Bulletin of the Seismological Society of America*, **63**, 615–622.

Chang, C., McNeill, L.C., Moore, J.C., Lin, W., Conin, M. & Yamada, Y. 2010. In situ stress state in the Nankai accretionary wedge estimated from borehole wall failures. *Geochemistry, Geophysics, Geosystems*, **11**, Q0AD04, https://doi.org/10.1029/2010GC003261

Chen, M.-A.P., Riedel, M., Spence, G.D. & Hyndman, R.D. 2008. Data report: A downhole electrical resistivity study of northern Cascadia marine gas hydrate. *In*: Riedel, M., Collett, T.S. & Malone, M.J. & the Expedition 311 Scientists (eds) *Proceedings of the Integrated Ocean Drilling Program, Volume 311*. Integrated Ocean Drilling Program Management International, Inc., Washington, DC, https://doi.org/10.2204/iodp.proc.311.203.2008

Christeson, G., Shipley, T., Gahagan, L., Johnson, K. & Davis, M. (eds). 2017. *Academic Seismic Portal (ASP) at UTIG*. University of Texas Institute for Geophysics, Austin, TX, http://www-udc.ig.utexas.edu/sdc/ [last accessed 24 May 2017]

Cochrane, G.R., MacKay, M.E., Moore, G.F. & Moore, J.C. 1994. Consolidation and deformation of sediments at the toe of the central Oregon accretionary prism from multichannel seismic data. *In*: Westbrook, G.K., Carson, B. *et al.* (eds) *Proceedings of the Ocean Drilling Program Initial Reports, Volume 146 (Part 1)*. Ocean Drilling Program, College Station, TX, 421–426, https://doi.org/10.2973/odp.proc.ir.146-1.003.1994

Davis, E.E. & Hyndman, R.D. 1989. Accretion and recent deformation of sediments along the northern Cascadia subduction zone. *Geological Society of America Bulletin*, **101**, 1465–1480.

Davis, E.E., Currie, R.G. & Sawyer, B.S. 1987. *Marine Geophysical Maps of Western Canada*. Geological Survey of Canada, Maps, 2-1987–17-1987.

DeMets, C., Gordon, R.G. & Argus, D.F. 2010. Geologically current plate motions. *Geophysical Journal International*, **181**, 1–80.

Flueh, E., Fisher, M.A. *et al.* 1998. New seismic images of the Cascadia subduction zone from cruise SO108 – ORWELL. *Tectonophysics*, **293**, 69–84.

Goldberg, D. & Janik, A. 2006. Data report: Stress orientation in gas hydrate–bearing sediments near Hydrate Ridge: evidence from borehole breakouts observed from logging-while-drilling resistivity images. *In*: Tréhu, A.M., Bohrmann, G., Torres, M.E. & Colwell, F.S. (eds) *Proceedings of ODP Scientific Results, Volume 2014*. Ocean Drilling Program, College Station, TX, 1–14.

Goldfinger, C., Kulm, L.D. *et al.* 1992. *Neotectonic Map of the Oregon Continental Margin and Adjacent Abyssal Plain*. State of Oregon, Department of Geology and Mineral Industries, Open File Report, **O-92-04**.

Goldfinger, C., Kulm, L.D., Yeats, R.S., Applegate, B., MacKay, M. & Cochrane, G.R. 1996. Active strike-slip faulting and folding of the Cascadia plate boundary and forearc in central and northern Oregon. *In*: Rogers, A.M., Walsh, T.J., Kockelman, W.J. & Priest, G. (eds) *Assessing and Reducing Earthquake Hazards in the Pacific Northwest*. United States Geological Survey, Professional Papers, **1560**, 223–256.

Goldfinger, C., Kulm, L.D., Yeats, R.S., McNeill, L.C. & Hummon, C. 1997. Oblique strike-slip faulting of the central Cascadia submarine forearc. *Journal of Geophysical Research*, **102**, 8217–8243.

Goldfinger, C., Kulm, L., McNeill, L.C. & Watts, P. 2000. Super-scale failure of the southern Oregon Cascadia Margin. *Pure and Applied Geophysics*, **157**, 1189–1226, https://doi.org/0033-4553/00/081189-38

Goldfinger, C., Nelson, C.H. *et al.* 2012. *Turbidite Event History: Methods and Implications for Holocene Paleoseismicity of the Cascadia Subduction Zone*. United States Geological Survey, Professional Papers, **1661-F**.

Grim, M.S., Coddington, J.M., Ambroziak, R.A. & McFaul, E.J. 1991. *GLORIA Imagery and Bathymetry from the U.S. EEZ off Washington, Oregon, and California*. United States Geological Survey, Open-File Report, **91-396**.

Hamilton, T.S., Enkin, R., Riedel, M., Rogers, G.C., Pohlman, J.W. & Benway, H.M. 2015. Slipstream: an early Holocene slump and turbidite record from the frontal ridge of the Cascadia accretionary wedge off western Canada and paleoseismic implications. *Canadian Journal of Earth Sciences*, **52**, 405–430.

Holbrook, W.S., Kent, G.M., Keranen, K.M., Johnson, H.P., Tréhu, A.M., Tobin, H.J., Caplan-Auerbach, J. & Beeson, J. 2012. Cascadia fore arc seismic survey: open access data. *American Geophysical Union*, **93**, 521–532. Available online at: http://steveholbrook.com/research/cascadia2d/eos-article-december-2012.pdf

Hyndman, R.D. 1995. The Lithoprobe corridor across the Vancouver Island continental margin: the structural and tectonic consequences of subduction. *Canadian Journal of Earth Sciences*, **32**, 1777–1802, https://doi.org/10.1139/e95-138

Hyndman, R.D. & Rogers, G.C. 2010. Great earthquakes on Canada's west coast: a review. *Canadian Journal of Earth Sciences*, **47**, 801–820.

Hyndman, R.D., Wang, K., Yuan, T. & Spence, G.D. 1993. Tectonic sediment thickening, fluid expulsion, and the thermal regime of subduction zone accretionary prisms: the Cascadia margin off Vancouver Island. *Journal of Geophysical Research*, **98**, 21 865–21 876.

Kelley, D. & Delaney, J. 2005. *Vancouver Island Mapping cruise TN-175, November 7–14, 2005*. University of Washington, Seattle, WA.

Knudson, K.P. & Hendy, I.L. 2009. Climatic influences on sediment deposition and turbidite frequency in the Nitinat Fan, British Columbia. *Marine Geology*, **262**, 29–38, https://doi.org/10.1016/j.margeo.2009.03.002

Lopez, C., Spence, G.D., Hyndman, R.D. & Kelley, D. 2010. Frontal ridge slope failure at the northern Cascadia margin: margin-normal fault and gas hydrate control. *Geology*, **38**, 967–970.

MacKay, M.E. 1995. Structural variation and landward vergence at the toe of the Oregon accretionary prism. *Tectonics*, **14**, 1309–1320, https://doi.org/10.1029/95TC02320

MacKay, M.E., Moore, G.F., Cochrane, G.R., Moore, J.C. & Kulm, L.D. 1992. Landward vergence and oblique structural trends in the Oregon margin accretionary prism: implications and effect on fluid flow. *Earth and Planetary Science Letters*, **109**, 447–491.

McAdoo, B.G. & Watts, P. 2004. Tsunami hazard from submarine landslides on the Oregon continental slope. *Marine Geology*, **203**, 235–245, https://doi.org/10.1016/S0025-3227(03)00307-4

McAdoo, B.G., Orange, D.L., Screaton, E., Lee, H. & Kayen, R. 1997. Slope basins, headless canyons, and submarine palaeoseismology of the Cascadia accretionary complex. *Basin Research*, **9**, 313–324, https://doi.org/10.1046/j.1365-2117.1997.00049.x

McAdoo, B.G., Pratson, L.F. & Orange, D.L. 2000. Submarine landslide geomorphology, US continental slope. *Marine Geology*, **169**, 103–136.

Moore, J.C., Moran, K., MacKay, M.E. & Tobin, H. 1995. Frontal thrust, Oregon accretionary prism: geometry, physical properties, and fluid pressure. *In*: Carson, B., Westbrook, G.K., Musgrave, R.J. & Suess, E. (eds) *Proceedings of the Ocean Drilling Program Scientific Results, Volume 146 (Part 1)*. Ocean Drilling Program, College Station, TX, 359–366, https://doi.org/10.2973/odp.proc.sr.146-1.224.1995

Moore, G., Cochrane, G., Tréhu, A. & Moore, C. 2015. Multi-channel seismic shot data from the Cascadia region of the Eastern North Pacific Ocean acquired during the R/V Geotide expedition GT8909 1989 (Version 1). *Integrated Earth Data Applications*, https://doi.org/10.1594/ieda/31956

Mulder, T. & Cochonat, P. 1996. Classification of offshore mass movements. *Journal of Sedimentary Research*, **66**, 43–57, https://doi.org/10.1306/D42682AC-2B26-11D7-8648000102C1865D

Orange, D.L. & Breen, N.A. 1992. The effects of fluid escape on accretionary wedges 2. Seepage force, slope failure, headless submarine canyons, and vents. *Journal Geophysical Research*, **97**, 9277–9295, https://doi.org/10.1029/92JB00460

Rial, J.A., Saltzman, N.G. & Ling, H. 1992. Earthquake-induced resonance in sedimentary basins. *American Scientist*, **80**, 566–578.

Riedel, M., Collett, T.S., Malone, M.J. & the Expedition 311 Scientists (eds). 2006. *Proceedings of the Integrated Ocean Drilling Program, Volume 311*. Integrated Ocean Drilling Program Management International, Inc., Washington, DC, https://doi.org/10.2204/iodp.proc.311.2006

Riedel, M., Collett, T.S. & Malone, M. 2010. Expedition 311 synthesis: scientific findings. *In*: Riedel, M., Collett, T.S., Malone, M.J. & the Expedition 311 Scientists (eds) *Proceedings of the Integrated Ocean Drilling Program, Volume 311*. Integrated Ocean Drilling Program Management International, Inc., Washington, DC, https://doi.org/10.2204/iodp.proc.311.213.2010

Riedel, M., Malinverno, A., Wang, K., Goldberg, D. & Guerin, G. 2016*a*. Horizontal compressive stress regime on the northern Cascadia margin inferred from borehole breakouts. *Geochemistry, Geophysics, Geosystems*, **17**, 3529–3545, https://doi.org/10.1002/2016GC006443

Riedel, M., Naegeli, K. & Côté, M.M. 2016*b*. *Assessment of Slope Failures off Vancouver Island Revealed in EM300 Multibeam Bathymetry Data*. Geological Survey of Canada, Open File Report, **8008**.

Rogers, G.C. 1988. An assessment of the megathrust earthquake potential of the Cascadia subduction zone. *Canadian Journal of Earth Sciences*, **25**, 844–852.

Ryan, W.B.F., Carbotte, S.M. *et al.* 2009. Global Multi-Resolution Topography synthesis. *Geochemistry, Geophysics, Geosystems*, **10**, Q03014, https://doi.org/10.1029/2008GC002332

Satake, K., Shimazaki, K., Tsuji, Y. & Ueda, K. 1996. Time and size of a giant earthquake in Cascadia inferred from Japanese tsunami records of January 1700. *Nature*, **379**, 246–249.

Satake, K., Wang, K. & Atwater, B.F. 2003. Fault slip and seismic moment of the 1700 Cascadia earthquake inferred from Japanese tsunami descriptions. *Journal of Geophysical Research*, **108**, 2535, https://doi.org/10.1029/2003JB002521

Sawyer, D.E., Flemings, P.B., Buttles, J. & Mohrig, D. 2012. Mudflow transport behavior and deposit morphology: role of shear stress to yield strength ratio in subaqueous experiments. *Marine Geology*, **307**, 28–39.

Scherwath, M., Riedel, M., Spence, G.D. & Hyndman, R.D. 2006. Data report: seismic structure beneath the north Cascadia drilling transect of IODP Expedition 311. *In*: Riedel, M., Collett, T.S., Malone, M.J. & the Expedition 311 Scientists (eds) *Proceedings of the Integrated Ocean Drilling Program, Volume 311*. Integrated Ocean Drilling Program Management International, Inc., Washington, DC, https://doi.org/10.2204/iodp.proc.311.110.2006

Scholz, N. 2013. *Submarine landslides offshore Vancouver Island, British Columbia and the possible role of gas hydrates in slope stability*. PhD thesis, University of Victoria, Victoria, BC, Canada.

Scholz, N.A., Riedel, M., Urlaub, M., Spence, G.D. & Hyndman, R.D. 2016. Submarine landslides along the northern Cascadia margin, offshore Vancouver Island, British Columbia: why preconditioning is likely required to trigger slope failure. *Geo-Marine Letters*, **36**, 323–337, https://doi.org/10.1007/s00367-016-0452-8

Semblat, J.F., Kham, M., Parara, E., Bard, P.Y., Pitilakis, K., Makra, K. & Raptakis, D. 2005. Site effects: basin geometry vs soil layering. *Soil Dynamics and Earthquake Engineering*, **25**, 529–538.

Sultan, N., Cochonat, P., Foucher, J.P. & Mienert, J. 2004. Effect of gas hydrates melting on seafloor slope instability. *Marine Geology*, **213**, 379–401.

ten Brink, U.S., Lee, H.J., Geist, E.L. & Twichell, D. 2009. Assessment of tsunami hazard to the US East Coast using relationships between submarine landslides and earthquakes. *Marine Geology*, **264**, 65–73.

Torres, M.E., Tréhu, A.M. *et al.* 2008. Methane hydrate formation in turbidite sediments of northern Cascadia IODP Expedition 311. *Earth and Planetary Science Letters*, **271**, 170–180.

Tréhu, A.M., Bohrmann, G. *et al.* 2003. *Proceedings of the Ocean Drilling Program, Volume 204. Initial Reports, Drilling Gas Hydrates on Hydrate Ridge, Cascadia Continental Margin*. Ocean Drilling Program, College Station, TX, https://doi.org/10.2973/odp.proc.ir.204.2003

Tréhu, A.M., Bohrmann, G. *et al.* 2004. Three-dimensional distribution of gas hydrate beneath southern Hydrate Ridge: constraints from ODP Leg 204. *Earth and Planetary Science Letters*, **227**, 557–558.

Twichell, D.C., Chaytor, J.D., ten Brink, U.S. & Buczkowski, B. 2009. Morphology of late Quaternary submarine landslides along the U.S. Atlantic continental margin. *Marine Geology*, **264**, 4–15.

Yuan, T., Hyndman, R.D., Spence, G.D. & Desmos, B. 1996. Seismic velocity increase and deep-sea gas hydrate concentration above a bottom-simulating reflector on the northern Cascadia continental slope. *Journal of Geophysical Research*, **101**, 13 665–13 671.

Yuan, T., Spence, G.D., Hyndman, R.D., Minshull, T.A. & Singh, S.C. 1999. Seismic velocity studies of a gas hydrate bottom-simulating reflector on the northern Cascadia continental margin: amplitude modeling and full waveform inversion. *Journal of Geophysical Research*, **104**, 1179–1191.

Yelisetti, S., Spence, G.D. & Riedel, M. 2014. Role of gas hydrates in slope failure on frontal ridge of northern Cascadia margin. *Geophysical Journal International*, **199**, 441–458.

Yelisetti, S., Spence, G.D., Scherwath, M., Riedel, M. & Klaeschen, D. 2017. Dual-vergence structure from multiple migration of widely spaced OBSs. *Tectonophysics*, **718**, 45–60, https://doi.org/10.1016/j.tecto.2017.04.005

Westbrook, G.K., Carson, B. *et al.* 1994. *Proceedings of the Ocean Drilling Program, Volume 146. Initial Reports Part 1: Cascadia Margin*. Ocean Drilling Program, College Station, TX, https://doi.org/10.2973/odp.proc.ir.146-1.1994